ARTICLES
https://doi.org/10.1038/s41929-021-00679-x

nature catalysis

Bimetallic monolayer catalyst breaks the activity–selectivity trade-off on metal particle size for efficient chemoselective hydrogenations

Qiaoqiao Guan[1,5], Chuwei Zhu[1,5], Yue Lin[2], Evgeny I. Vovk[3], Xiaohong Zhou[3], Yong Yang[3], Hancheng Yu[1], Lina Cao[2], Hengwei Wang[2], Xiaohui Zhang[1], Xinyu Liu[1], Mengkai Zhang[1], Shiqiang Wei[4], Wei-Xue Li[1,2] ✉ and Junling Lu[1,2] ✉

Particle size governs the geometric and electronic structure of metal nanoparticles (NPs), shaping their catalytic performance. However, size-dependent entanglement in the geometric and electronic structures often leads to a trade-off between activity and selectivity, limiting the optimization of the overall catalytic performance. Here we show that precisely controlled deposition of a platinum monolayer on large gold NPs breaks the activity–selectivity trade-off on particle size in platinum-catalysed chemoselective hydrogenation of halonitrobenzenes, resulting in a remarkable activity, along with a 99% selectivity for haloanilines under mild conditions. The high activity results from upshift of the platinum 5*d*-band centre through platinum lattice expansion and ligand effect, whereas the high selectivity is caused by exposing more terrace sites on large particles. The geometric and electronic properties of bimetallic monolayer materials, distinct from monometallic NPs and alloys, constitute a promising platform for the rational design of metal catalysts with superior performance in hydrogenation reactions.

Metal nanoparticle (NP) catalysts are widely used in various catalytic reactions including chemical refining, automotive exhaust treatment and biomass conversions. Changes in the particle size in the nanoscale regime affect substantially both the geometric structures of NPs, in terms of fractions of low- and high-coordination sites (LCSs and HCSs), and their inherent electronic structures due to the prominent quantum effect. The distinct characteristics and great flexibility of both the geometric and electronic structures of NPs provide a large phase space to impact the chemistry of breaking and making chemical bonds, which has essentially driven the development of nanocatalysts for decades[1–9]. However, simultaneous changes in both geometric and electronic structures along with the particle size often lead to an activity–selectivity trade-off in many catalytic reactions, obscuring efforts to optimize the performance of nanocatalysts. Bimetallic catalysts provide a different dimension to tune the geometric and electronic properties via the characteristic strain and ligand effect for catalysis.[10,11] Properties resulting in activity and selectivity changes on bimetallic catalysts with respect to monometallic nanoparticles are important for rational design of new catalysts but have not been explored in depth.

Hydrogenation is an important and widely applied class of metal-catalysed reactions in which high selectivity is generally achieved only at the expense of activity despite extensive investigations having been performed for decades[12–14]. In particular, achieving high chemoselectivity at high activity represents a great challenge because the hydrogenation of competing functional substitute groups can occur simultaneously. For example, in chemoselective hydrogenation of halonitrobenzenes (HNBs) with molecular H_2 to produce haloanilines (HANs)—key intermediates for pharmaceuticals, polymers, agrochemicals and dyes[15,16]—platinum group metals[17–21] often show high activities, but low selectivity for HANs because hydrogenolysis of the carbon–halogen bonds often occurs on these active catalysts to generate dehalogenated aniline (AN) by-products, especially at high conversions. Although increasing the particle size of platinum NPs improves the selectivity of *para*-chloroaniline (*p*-CAN), the activity and metal efficiency of these precious metals are both substantially decreased[22]. Gold-[23,24] and silver-based[25,26] catalysts can hydrogenate the nitro group with high chemoselectivity, but require very harsh conditions due to their low activity of H_2 dissociation[27]. For example, Corma and co-workers reported that a PtAu bimetallic catalyst showed a considerably higher activity than gold NPs, but was still much less active than the platinum monometallic counterpart[13,27]. Partially poisoning the metal sites with additives such as thiols is another effective way to improve the selectivity, but again decreases the activity considerably[28]. So far none of these approaches have achieved high chemoselectivity and high activity simultaneously.

In this article we show that for Pt/SiO_2-catalysed hydrogenation of HNBs, the activity and selectivity exhibit a see-saw relationship with platinum particle sizes from 1.1 to 9.3 nm. Specifically, the highest activity occurs on 2.7 nm platinum NPs but the corresponding selectivity is lowest, whereas the highest selectivity occurs at 1.1 and 9.3 nm NPs but the corresponding activity is very low, a fact that severely limits the improvement of HAN production with high selectivity. Density functional theory (DFT) calculations revealed that this limitation stems from the size-dependent entanglement of

[1]School of Chemistry and Materials Science, Key Laboratory of Surface and Interface Chemistry and Energy Catalysis of Anhui Higher Education Institutes, University of Science and Technology of China, Hefei, China. [2]Hefei National Laboratory for Physical Sciences at the Microscale, University of Science and Technology of China, Hefei, China. [3]School of Physical Science and Technology, ShanghaiTech University, Shanghai, China. [4]National Synchrotron Radiation Laboratory, University of Science and Technology of China, Hefei, China. [5]These authors contributed equally Q. Guan, C. Zhu. ✉e-mail: wxli70@ustc.edu.cn; junling@ustc.edu.cn

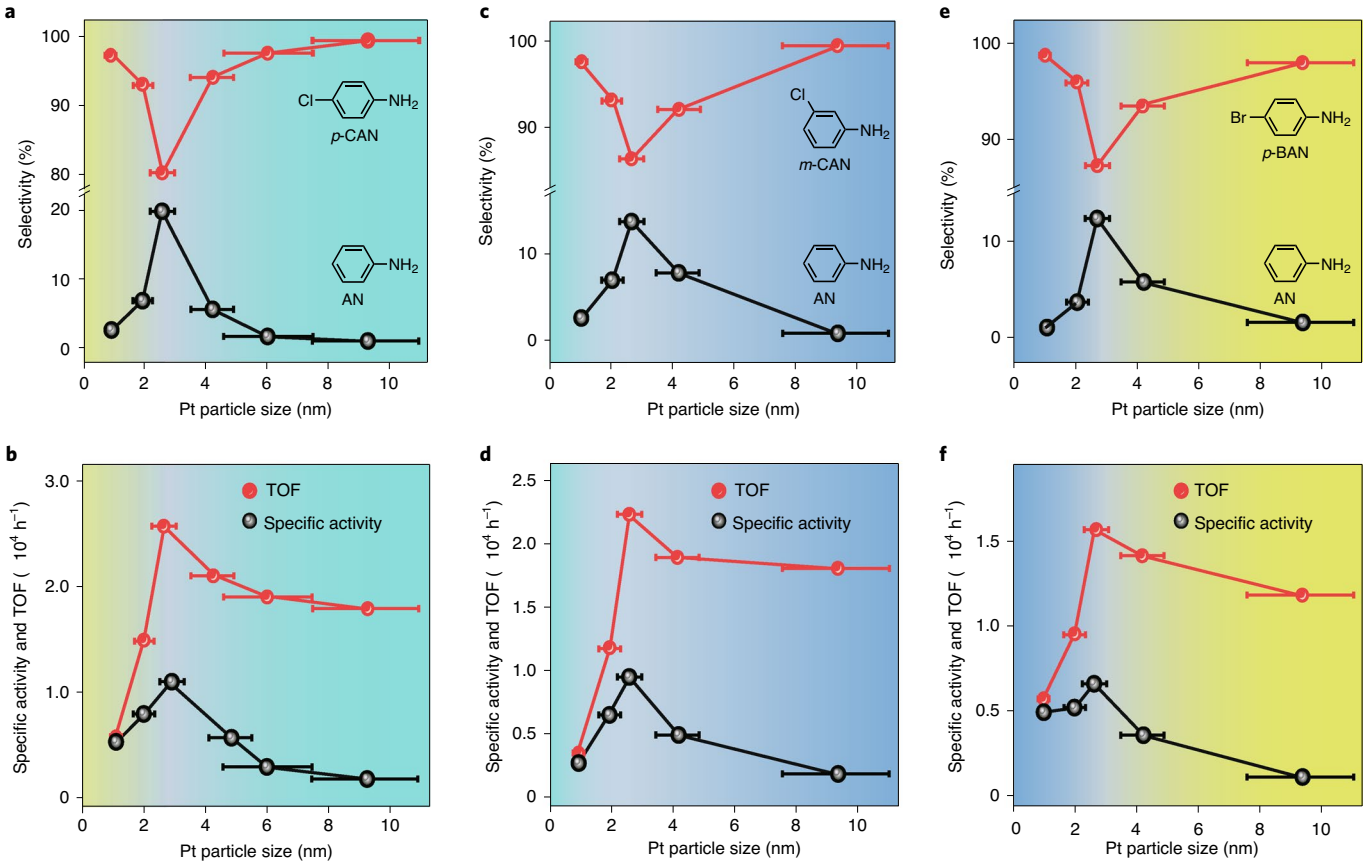

Fig. 1 | Catalytic performance of Pt/SiO_2 catalysts in the hydrogenation of HNBs. a,**b**, Selectivity to *p*-CAN and AN (**a**) and corresponding TOFs and specific activities (**b**) for platinum NPs ranging in size from 1.1 to 9.3 nm for the hydrogenation of *p*-CNB. **c**,**d**, Selectivity to *m*-CNB and AN (**c**) and the corresponding TOFs and specific activities (**d**) for platinum NPs ranging in size from 1.1 to 9.3 nm for the hydrogenation of *m*-CNB. **e**,**f**, Selectivity to *p*-BNB and AN (**e**) and the corresponding TOFs and specific activities (**f**) for platinum NPs ranging in size from 1.1 to 9.3 nm for the hydrogenation of *p*-BAN. Error bars represent the standard deviations of platinum particle size of Pt/SiO_2 catalysts as determined by TEM. Reaction conditions: solvent, ethanol (40 ml); H_2 pressure, 0.3 MPa; temperature, 65 °C; platinum/substrate mole ratio, 1:7,800, where the substrate was either *p*-CNB (8 mmol), *m*-CNB (8 mmol) or *p*-BNB (6 mmol).

HCS/LCS ratios and Fermi levels of platinum NPs, and predicted that bimetallic monolayer platinum on Au(111)—with upshift of the platinum 5*d*-band centre leading to higher activity and with flat terrace sites leading to high selectivity—would enable the activity–selectivity see-saw to be broken. Guided by theory, a core–shell bimetallic Au@Pt/SiO_2 catalyst with a monolayer platinum shell (Au@1ML-Pt), precisely fabricated using atomic layer deposition (ALD), exhibited 99% selectivity to HANs and superior activity, demonstrating the great advantages of bimetallic monolayer catalysts for modulating geometric and electronic structures when performing hydrogenations.

Results

Platinum particle size effect in hydrogenation of HNBs. Pt/SiO_2 catalysts with various platinum particle sizes from 1.1 to 9.3 nm (denoted as *x* nm-Pt, where *x* is the average particle size) and platinum loadings varying from 0.8 to 3.5 wt% were first synthesized using ALD[29] (Supplementary Figs. 1 and 2 and Supplementary Table 1) and evaluated for selective hydrogenation of *para*-chloronitrobenzene (*p*-CNB) in a stainless steel batch reactor. A stirring speed of 1,500 r.p.m. was used to ensure the evaluation of catalytic performance in the kinetic region without any external diffusion or heat limitation (Supplementary Figs. 3 and 4). The 9.3 nm-Pt sample showed a high selectivity of 99% to *p*-CAN at 100% *p*-CNB conversion (Fig. 1a and Supplementary Fig. 5); the turnover frequency (TOF) based on the number of surface platinum atoms was $1.80\times10^4\,h^{-1}$ and the specific activity based on the total platinum content was $0.17\times10^4\,h^{-1}$ (Fig. 1b). Reducing the platinum particle size to 2.7 nm considerably increased the TOF and specific activity to 2.58×10^4 and $1.09\times10^4\,h^{-1}$, respectively, but decreased the *p*-CAN selectivity substantially to 80%; thus a considerable amount of dehalogenated AN by-product was generated. A further decrease in the platinum particle size to 1.1 nm increased the *p*-CAN selectivity back to 98%, whereas the TOF and specific activity dropped substantially to 0.60×10^4 and $0.52\times10^4\,h^{-1}$, respectively. This activity–selectivity see-saw with particle size is not related to the coverage of substrate (Supplementary Fig. 6). Kinetic studies further showed the apparent activation energy changed inversely with platinum particle size, agreeing excellently with the trend of activity (Supplementary Fig. 7).

Similar phenomena were also observed in the selective hydrogenation of *meta*-chloronitrobenzene (*m*-CNB) and *para*-bromonitrobenzene (*p*-BNB) (Fig. 1c–f), where we again found that the 2.7 nm-Pt catalyst was the inflection point for both activity and selectivity. Compared to hydrogenation of *p*-CNB, the specific activity of 2.7 nm-Pt for hydrogenation of *m*-CNB and *p*-BNB deceased to 9,423 and $6{,}581\,h^{-1}$, respectively. In brief, the activity–selectivity see-saw with platinum particle size manifests the dilemma of platinum size variation in improving the catalytic performance in chemoselective hydrogenation of HNBs.

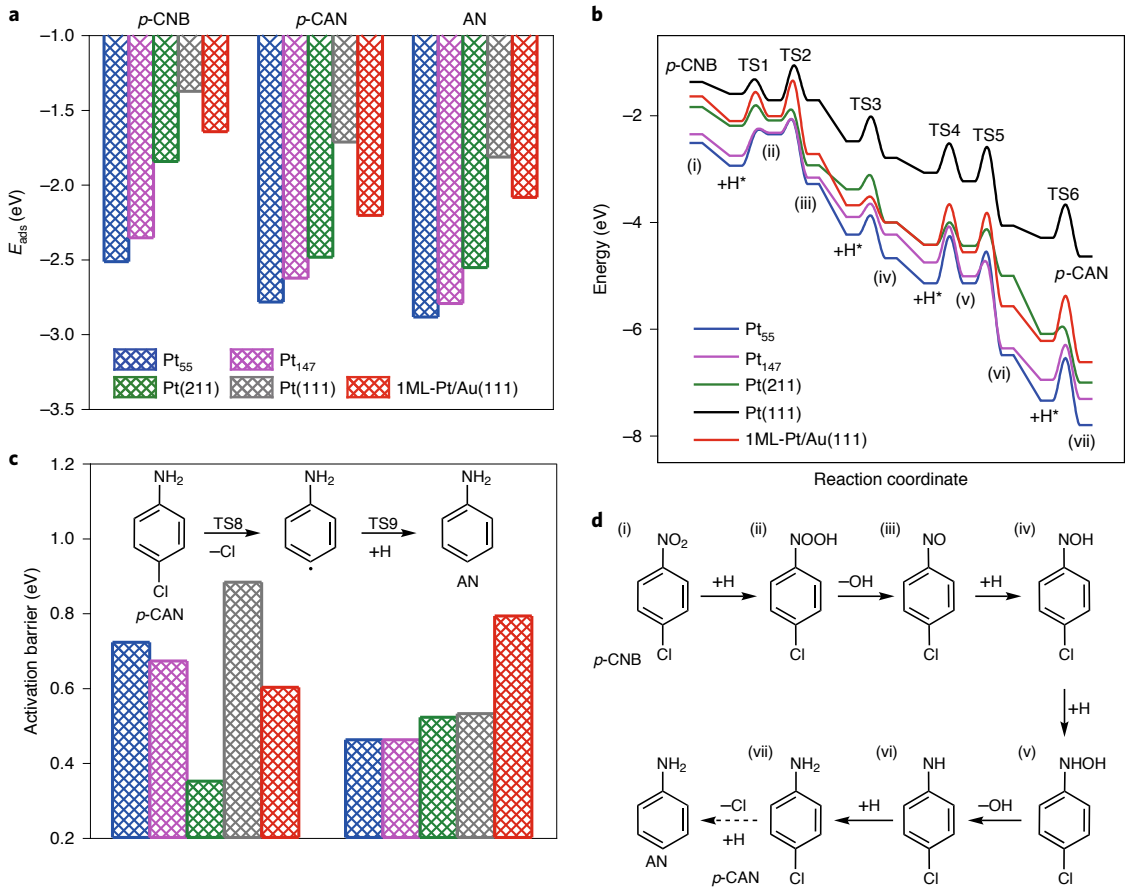

Fig. 2 | Calculated parameters of hydrogenation of *p*-CNB on platinum surfaces. a, Adsorption energies of *p*-CNB, *p*-CAN and AN on Pt_{55}, Pt_{147}, Pt(211), Pt(111) and 1ML-Pt/Au(111). **b**, Potential energy profiles of *p*-CNB hydrogenation to form *p*-CAN on these five surfaces. **c**, Calculated activation barriers for *p*-CAN dechlorination to AN on these five surfaces. **d**, The corresponding intermediate states in **b**.

Theoretical insight of platinum particle size effect. To shed light on the activity–selectivity see-saw with platinum particle size and to rationally design a more efficient metal catalyst, DFT calculations were performed on flat Pt(111), stepped Pt(211), Pt_{147} and Pt_{55} clusters (Supplementary Fig. 8), which represent terrace and edge/corner sites of larger platinum NPs and smaller NPs of ~1.6 and ~1.1 nm used in experiments, respectively. We first compared the adsorption of *p*-CNB, *p*-CAN and AN on these surfaces and found that the adsorption energies of these three molecules were generally exothermic and above −1.35 eV, in the order AN > *p*-CAN > *p*-CNB, regardless of surface (Fig. 2a and Supplementary Fig. 9). The bonding strengths on these surfaces exhibit a similar trend for all these molecules: $Pt_{55} > Pt_{147} > Pt(211) > Pt(111)$. Considerably stronger adsorptions on Pt_{55} and Pt_{147} are due mainly to their lowered work function (or higher Fermi level) and accordingly enhanced charge transfers between platinum clusters and substrates (Supplementary Fig. 10), in line with previous work[9,30,31]. Reinforced electron transfer on smaller particles stems from more metal atoms besides the coordinated ones contributing electrons to a greater extent (Supplementary Fig. 11).

As shown in Supplementary Table 2, the calculated activation barriers of the elementary steps in *p*-CNB hydrogenation to *p*-CAN on these surfaces are all modest and less than 1 eV. In contrast, adsorptions and reaction energies vary to a much larger extent on different catalysts (Fig. 2b), and thus would play more important roles in the overall reactivity and selectivity. In this context, the potential energy surface (PES) of *p*-CNB hydrogenation on Pt(111) lies on the top, over all the other surfaces (Fig. 2b and Supplementary Fig. 12). Namely, all binding strengths of reactant, intermediates and products to Pt(111) involved are relatively weak, and the whole hydrogenation process is less exothermic, suggesting a relatively low activity of Pt(111) in *p*-CNB hydrogenation.

The adsorption of *p*-CNB on Pt(211) is −1.84 eV, which is much stronger than that on Pt(111) (−1.37 eV), and the reaction process also becomes more exothermic (green curve in Fig. 2b and Supplementary Fig. 13). Meanwhile, the barriers of the elementary steps involved are also lower than those on Pt(111) (Supplementary Table 2), and these together result in Pt(211) being more active. We note that when reducing the platinum particle size in the cuboctahedron shape from 9.3 to 2.7 nm, the ratio of HCSs to LCSs decreases substantially from 6.8 to 2.0 (Supplementary Fig. 14). The higher intrinsic activity of Pt(211) than Pt(111) excellently explains the trend of activity found experimentally on platinum NPs larger than 2.7 nm (Fig. 1b), illustrating the dominant role of the geometric effect on the activity of large platinum NPs.

The PESs of Pt_{55} and Pt_{147} clusters lying at the bottom demonstrate their overall high binding strengths toward adsorbates and reaction intermediates. However, the very strong adsorptions of *p*-CNB on Pt_{55} (−2.51 eV) and Pt_{147} (−2.35 eV) cause the first hydrogenation step of *p*-CNB to $C_6H_4ClNOOH^*$ to become endothermic with higher elementary reaction barriers (Fig. 2b,d, step ii, and Supplementary Figs. 15 and 16) than with Pt(111). Moreover, the substantially stronger adsorption of *p*-CAN on Pt_{55} (−2.78 eV) and Pt_{147} (−2.62 eV) than on Pt(111) (−1.71 eV) retards the

desorption of *p*-CAN product, further lowering the overall activity. Compared to Pt_{55}, the barriers of elementary steps on Pt_{147} are lower (Supplementary Table 2), indicating that the activity of Pt_{147} is higher than that of Pt_{55}. It appears that this overbound adsorption on Pt_{55} and Pt_{147}, caused mainly by the electronic effect, is responsible for the decreased activity when reducing the platinum particle size from 2.7 to 1.1 nm (Fig. 1).

To understand the change in selectivity with platinum particle size, we calculated the cleavage of the C–Cl bond in *p*-CAN (equation (1)) and the subsequent hydrogenation (equation (2)).

$$C_6H_4ClNH_2 * + \square \rightarrow C_6H_4NH_2 * + Cl* \quad (1)$$

$$C_6H_4NH_2 * + H* \rightarrow C_6H_5NH_2 * + \square \quad (2)$$

Here ▢ denotes an available surface site. The barriers for these two elementary steps on these three surfaces are shown in Fig. 2c. We found that dechlorination of *p*-CAN on Pt(111) is endothermic by 0.35 eV with a considerable barrier of 0.88 eV (Supplementary Table 2). In contrast, these two steps on Pt(211) become exothermic by at least −0.77 eV along with low barriers of 0.35 and 0.52 eV, respectively. Large improvement on reaction energies by more than 1 eV and corresponding kinetics come largely from the enhanced binding of the products on Pt(211) (Supplementary Table 3). Therefore, dechlorination of *p*-CAN preferentially occurs on stepped Pt(211) surfaces, and hence larger platinum NPs have a higher *p*-CAN selectivity in excellent agreement with our experimental findings (Fig. 1a). For dechlorination of *p*-CAN on Pt_{147} and Pt_{55}, although the corresponding reaction energies remain exothermic (−0.52 and −0.65 eV) and similar to those on Pt(211), the large curvatures of these two small clusters require a greater stretching of the C–Cl bond (2.57 and 2.72 Å) to reach the transition state than required with Pt(211) (2.47 Å) (Supplementary Fig. 17). This raises the barriers to 0.67 and 0.72 eV, respectively, both higher than on Pt(211) (0.35 eV). This limits the dechlorination process and increases the *p*-CAN selectivity on small clusters, precisely as found experimentally for the platinum particle sizes below 2.7 nm (Fig. 1a).

Theoretical prediction of an active and selective catalyst. As discussed above, because the entanglement of HCS/LCS ratios and Fermi levels depends on particle size, variation of the platinum particle size alone cannot achieve high activity and chemoselectivity at the same time, as found in our previous palladium-catalysed aerobic oxidation of benzyl alcohol[30]. Bimetallic catalysts, whose unique strain and ligand effects provide another dimension to tune the geometric and electronic structures,[10,11] might overcome the entanglement effect that occurs when changing the particle size and resolve the activity–selectivity trade-off noted above. An AuPt alloy with an Au:Pt atomic ratio of 1:1 was first examined (Supplementary Fig. 18). We found that the adsorption energies of *p*-CNB, *p*-CAN and AN on this AuPt alloy were generally smaller than −1.35 eV, all much weaker than those on Pt(111) (Supplementary Table 3 and Supplementary Fig. 19). Therefore, a low activity could be expected and AuPt alloy is excluded.

The above calculations show that although Pt(111) is less active, its selectivity to desired *p*-CAN is high, manifesting the importance of terrace sites for the selectivity. Starting from this, we constructed a platinum monolayer on Au(111) (hereafter referred to as 1ML-Pt/Au(111)) for the reactivity study described below. Note that the gold underneath expands the lattice of the supported platinum layer from 2.77 to 2.89 Å by 4.3% (Supplementary Fig. 20). This lattice expansion and the orbital hybridization between platinum and gold induce a considerable upshift of the platinum 5*d*-band centre by 0.69 eV towards the Fermi level (Supplementary Fig. 21), which would make the exposed platinum overlayer more reactive. Indeed, the binding strengths of all reactants and intermediates of *p*-CNB hydrogenation on 1ML-Pt/Au(111) are improved (Supplementary Table 3). This lowers the overall PES close to that of Pt(211) (Fig. 2b and Supplementary Fig. 22), implying a higher activity of 1ML-Pt/Au(111)—even comparable to the activity of Pt(211). On the other hand, the reaction barrier for dechlorination of *p*-CAN on flat 1ML-Pt/Au(111) remains considerable at 0.60 eV (Fig. 2c), and the reaction energy is thermally neutral (−0.12 eV), similar to that of Pt(111) but contrasting that of Pt(211), which has a larger exothermic reaction energy of −0.79 eV. Together, these results indicate that a monolayer platinum shell on a large gold core with more flat facets exposed can achieve high activity and selectivity to *p*-CAN at same time.

Further calculations of the HNB derivatives show that the adsorption of *m*-CNB and *p*-CNB on these five surfaces is very similar to that of *p*-CNB, apart from becoming slightly stronger (Supplementary Figs. 23 and 24). Therefore, a similar improvement of both activity and selectivity can be expected for hydrogenation of *m*-CNB and *p*-BNB on a 1ML-Pt/Au(111) surface.

Synthesis and characterization of AuPt bimetallic catalysts. As guided by the above theoretical prediction, we synthesized Au@Pt core–shell bimetallic NPs with different platinum shell thicknesses. An Au/SiO_2 catalyst with a relative large gold particle size of 5.3 ± 0.7 nm (denoted as 5.3 nm-Au) was first synthesized using a deposition–precipitation method (Supplementary Fig. 25); next, platinum was selectively deposited onto the gold NPs by ALD with near-atomic precision control at 150 °C for 1, 3 and 8 cycles[32], producing Au@0.5ML-Pt, Au@1ML-Pt and Au@2ML-Pt, respectively, which yielded corresponding platinum loadings of 0.4, 0.9 and 1.9 wt%, as determined by inductively coupled plasma atomic emission spectroscopy (Supplementary Fig. 26 and Supplementary Table 4). X-ray diffraction measurements showed that there were four diffraction peaks on Au/SiO_2, located at 38.4°, 44.5°, 64.9° and 77.9°, assigned to Au(111), Au(200), Au(220) and Au (311), respectively. These peaks remained nearly intact in Au@0.5ML-Pt, Au@1ML-Pt and Au@2ML-Pt, indicating the formation of an Au@Pt core–shell structure instead of alloys (Fig. 3a). Transmission electron microscopy (TEM) measurements showed that the average particle size after platinum deposition was about 5.5 ± 0.7, 5.8 ± 0.7 and 6.4 ± 0.9 nm for Au@0.5ML-Pt, Au@1ML-Pt and Au@2ML-Pt, respectively, indicating a platinum shell growth rate of 0.07 nm per ALD cycle (Supplementary Figs. 25 and 27), close to the growth rate of platinum ALD reported in the literature[33]. According to the cuboctahedron cluster model[34], the thicknesses of platinum shells on 5.3 nm gold NPs after performing 1, 3 and 8 cycles of ALD were about 0.5, 1.0 and 2.1 monolayers, respectively (Supplementary Table 5). To further confirm the platinum shell thickness, we measured the platinum dispersions in these three bimetallic catalysts using CO as a probe molecule, and found that these were 100%, 91.9%, 54.8%, respectively (Fig. 3b), in excellent agreement with the corresponding platinum shell thicknesses determined by TEM. Aberration-corrected high-angle annular dark-field scanning TEM (HAADF-STEM) measurements of Au@1ML-Pt revealed that, although gold and platinum have barely any contrast in brightness, the distance between the outmost and second layers shrank by 6.8% relative to that of bulk, sharply different from the constant distance observed on blank 5.3 nm-Au particles, verifying the presence of a single platinum monolayer on gold NPs in Au@1ML-Pt (Fig. 3c and Supplementary Figs. 28 and 29). Meanwhile, the lattice distance within the platinum layer was ~2.86 Å, close to the underlying gold lattice, which expanded by 3.2% compared to bulk platinum (2.77 Å), consistent with the theoretical calculations (Supplementary Fig. 20). Similarly, HAADF-STEM of Au@2ML-Pt, found that the interplanar distance between the outmost and the second layers, and between the second and the third layers both

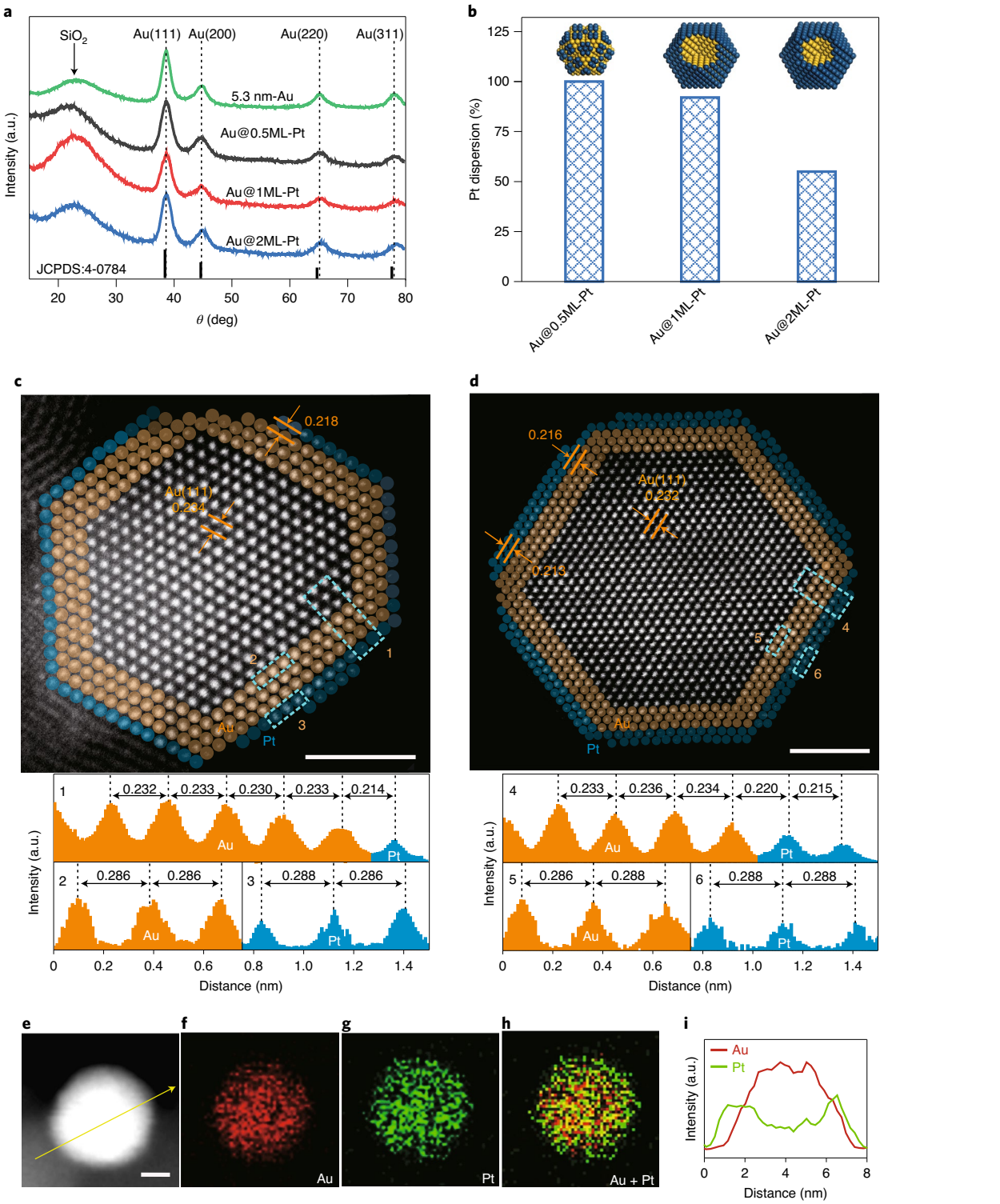

Fig. 3 | Morphology of Au@Pt core–shell catalysts. a, X-ray diffraction spectra of 5.3 nm-Au and Au@Pt bimetallic catalysts. **b**, Platinum dispersions of Au@Pt bimetallic catalysts as determined by CO chemisorption. The insets show the models of the corresponding Au@Pt core–shell catalysts, where the dark blue and yellow spheres are platinum and gold atoms, respectively. **c**,**d**, Representative atomic-resolution HAADF-STEM images of Au@1ML-Pt (**c**) and Au@2MLPt (**d**) catalysts, with the corresponding line intensity profiles along the numbered dashed rectangles to show the interplanar distance and the lattice distance. In **c** and **d**, the atoms in the outer layers are shown as light yellow and blue spheres to highlight the gold core and platinum shell. **e**–**h**, A STEM image of an Au@2ML-Pt particle (**e**) and the corresponding EDS mapping of Au (**f**), Pt (**g**), and Au + Pt (**h**) signals. **i**, Line profile of Au@2ML-Pt. The yellow arrow in **e** indicates the position for the line profile in **i**. The length of the scale bars in **c**, **d**, **e** are 2 nm.

shrank by ~0.03 Å, confirming the presence of two platinum monolayers on gold NPs (Fig. 3d and Supplementary Fig. 28). Meanwhile, the lattice expansion of the second platinum shell remained. Elemental mapping using energy-dispersive X-ray spectroscopy (EDS) and line profiles further confirmed the Au@Pt core–shell structure (Fig. 3e–i).

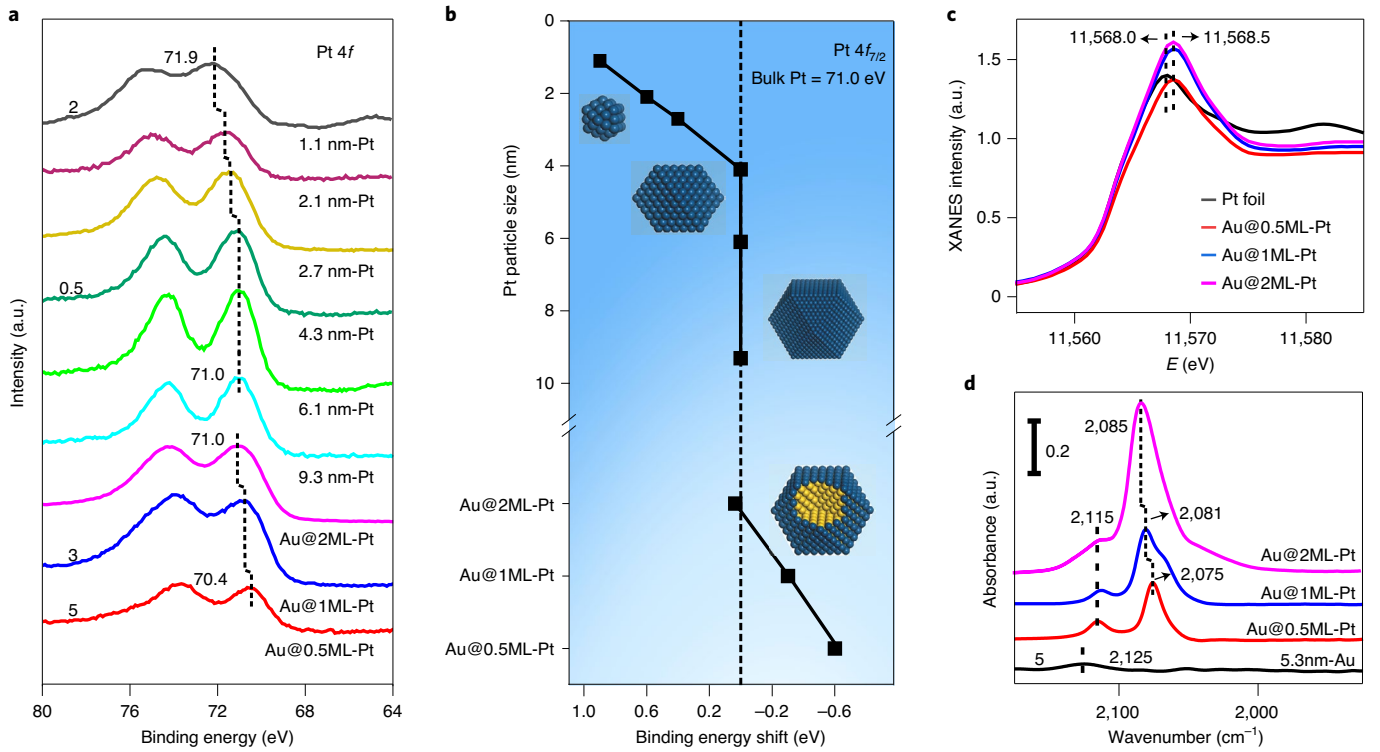

Fig. 4 | Electronic properties of platinum monometallic and Au@Pt core–shell catalysts. a, In situ XPS platinum 4*f* core level spectra taken after in situ reduction of all platinum monometallic and Au@Pt bimetallic core–shell catalysts. **b**, Highlight of the shifts of platinum $4f_{7/2}$ binding energy with platinum particle size and composition normalized to that of bulk platinum. The insets show models of different sizes of platinum NPs and Au@Pt bimetallic core–shell catalysts, where the dark blue and yellow spheres are platinum and gold atoms, respectively. **c**, XANE spectra of Au@0.5ML-Pt, Au@1ML-Pt, Au@2ML-Pt core–shell catalysts and platinum foil reference at the Pt L_3-edge. **d**, DRIFTS of CO chemisorption on Au@0.5ML-Pt, Au@1ML-Pt, Au@2ML-Pt bimetallic catalysts and Au/SiO_2 catalysts.

In situ X-ray photoemission spectroscopy (XPS) showed that the platinum $4f_{7/2}$ core level peak binding energies of the 9.3, 6.3 and 4.3 nm-Pt catalysts were nearly the same at 71.0 eV, identical to that of bulk metallic platinum (71.0 eV)[35] (Fig. 4a). Further decreasing the platinum particle size caused considerable shifts to higher binding energies up to 0.9 eV for the 1.1 nm-Pt catalyst, in line with literature findings[36]. The platinum $4f_{7/2}$ binding energy of Au@2ML-Pt was also 71.0 eV, which matches the bulk platinum value. In contrast, considerable shifts of 0.36 and 0.64 eV to lower binding energies were observed for Au@1ML-Pt and Au@0.5ML-Pt, respectively, implying charge transfers from gold to platinum atoms, in agreement with the literature[37]. The negative shift of platinum $4f_{7/2}$ binding energy for Au@0.5ML-Pt and Au@1ML-Pt is in contrast to the positive shift of monometallic platinum particles as demonstrated in Fig. 4b, suggesting an additional opportunity to tune catalytic performance besides particle size variation.

X-ray absorption near-edge structure (XANES) is also known for characterizing the electronic properties of adsorbing atoms[38,39]. For the XANE curve at the platinum L_3-edge, it is known that the area under the white line peak is proportional to the population of the unoccupied platinum 5*d* states[40,41]. Here we found that the intensities of white line peaks followed the order: Au@0.5ML-Pt < Au@1ML-Pt < Au@2ML-Pt (Fig. 4c), implying that the thinner platinum shell thickness had a lower population of unoccupied platinum 5*d* states, in line with the XPS observation. It should be noted that the higher absorption edge energy of 11,568.5 eV of Au@Pt bimetallic samples than that of platinum foil (11,568.0 eV) might be attributed to air exposure of platinum during ex situ measurements.

Infrared spectroscopy of CO chemisorption is another convenient tool to reveal the population of metal 5*d* electronic states[42–44]. Here diffuse reflectance infrared Fourier transform spectroscopy (DRIFTS) of CO chemisorption showed that there were two peaks located at 2,115 and 2,075 cm^{-1} on Au@0.5ML-Pt (Fig. 4d), assigned to linear CO on gold and platinum, respectively[45]. Increasing the platinum shell coverage caused the linear CO peak on platinum to exhibit blue shifts to 2,081 and 2,085 cm^{-1} on Au@1ML-Pt and Au@2ML-Pt, respectively. These results suggest that the platinum atoms in Au@0.5ML-Pt and Au@0.5ML-Pt have more populated 5*d* state electrons which strengthens the Pt(5*d*)–CO($2\pi^*$) bonding through π back-donation, resulting in lower CO vibrational frequencies[44,46]. In brief, the results of XPS, XANES and DRIFTS all coincided perfectly with each other, demonstrating the strong electronic interactions between platinum and gold in Au@Pt bimetallic catalysts, in line with the above theory.

Catalytic performance of AuPt bimetallic catalysts. In chemoselective hydrogenation of *p*-CNB, the 5.3 nm-Au catalyst showed a negligible activity due to its low capability of H_2 dissociation, in line with the literature (Fig. 5a)[27]. In sharp contrast, the Au@0.5ML-Pt catalyst exhibited a *p*-CAN selectivity of 99%, and the specific activity based on the platinum content was 1.75×10^4 $mol_{p\text{-CNB}} \cdot mol_{Pt}^{-1} h^{-1}$, higher than that of the most active sample of 2.7 nm-Pt. Au@1ML-Pt exhibited an even higher specific activity of 3.44×10^4 $mol_{p\text{-CNB}} \cdot mol_{Pt}^{-1} h^{-1}$. More importantly, the high *p*-CAN selectivity was successfully preserved at 99%. On Au@2ML-Pt, the specific activity decreased considerably to 2.60×10^4 $mol_{p\text{-CNB}} \cdot mol_{Pt}^{-1} h^{-1}$, while the high *p*-CAN selectivity was still retained. Kinetic experiments further showed a considerably lower reaction barrier of 24.2 kJ mol^{-1} for Au@1ML-Pt catalyst than that (34.9 kJ mol^{-1}) of 2.7 nm-Pt (Fig. 5b). Examination of Au@1ML-Pt in hydrodechlorination of chlorobenzene showed

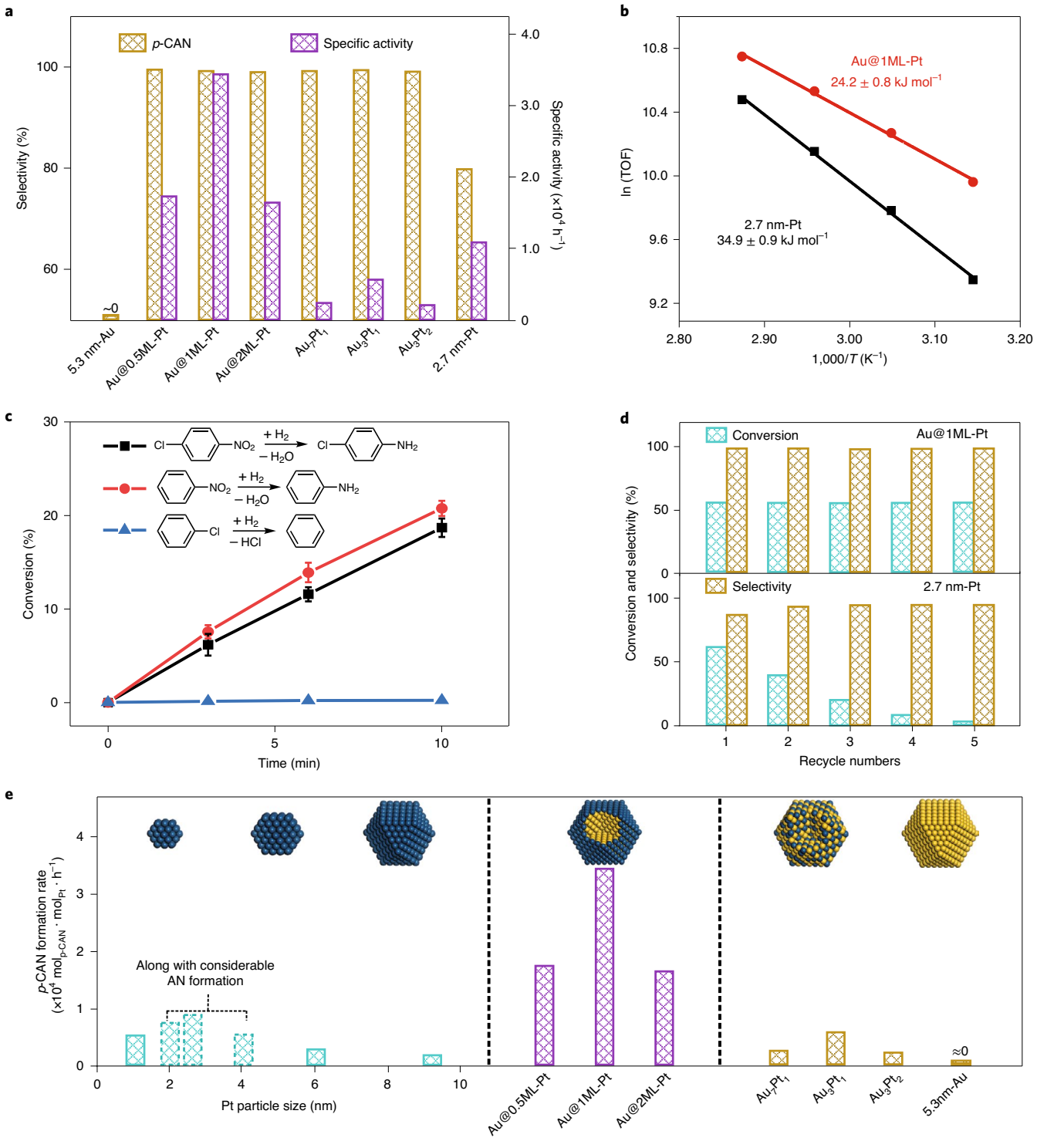

Fig. 5 | Comparison of catalytic performance of platinum-based catalysts in chemoselective hydrogenation of *p*-CNB. a, Comparison of selectivity to *p*-CAN and specific activities of Au@Pt core–shell and AuPt alloy bimetallic catalysts with 2.7 nm-Pt and 5.3 nm-Au monometallic catalysts. **b**, Arrhenius plots of Au@1ML-Pt and 2.7 nm-Pt catalysts for hydrogenation of *p*-CNB. **c**, Au@1ML-Pt for hydrogenation of *p*-CNB, NB and chlorobenzene. **d**, Comparison of the recyclability of Au@1ML-Pt and 2.7 nm-Pt catalysts. **e**, Comparison of the *p*-CAN formation rates on the platinum, gold, AuPt alloy and Au@Pt core–shell catalysts. Reaction conditions: solvent, ethanol (40 ml); H_2 pressure, 0.3 MPa; temperature, 65 °C; *p*-CNB, 8 mmol; platinum/substrate mole ratios, 1:7,800 for the catalysts used in **a** and **d**, 1:15,600 for 2.7 nm-Pt used in **b**, and 1:31,200 for Au@1ML-Pt used in **b** and **c**.

a negligible conversion under the same conditions, sharply different from the facile hydrogenation of the nitro group in both NB and *p*-CNB (Fig. 5c and Supplementary Fig. 30), further validating the high chemoselectivity. These experimental results are in excellent agreement with the above theoretical prediction of the win–win scenario of high activity and chemoselectivity on 1ML-Pt/Au(111).

More importantly, the optimized Au@1ML-Pt catalyst also showed a much better recyclable stability than that of 2.7 nm-Pt (Fig. 5d). Chlorine poisoning induced by the dechlorination path, and considerable agglomeration and leaching of platinum particles, are found to be the major reasons for the deactivation of 2.7 nm-Pt catalyst (Supplementary Figs. 31 and 32 and Supplementary Table 6).

As a control experiment, we also reduced the three Au@Pt core–shell bimetallic catalysts at 550 °C in 10% H_2 in Ar for 30 min to form Au_7Pt_1, Au_3Pt_1 and Au_3Pt_2 alloy catalysts, as confirmed by the gradual shift of the X-ray diffraction peak of Au(111) from 38.4° to 39.1° (Supplementary Fig. 33). TEM showed there was no obvious change in metal particle size (Supplementary Fig. 34). When hydrogenating *p*-CNB, we found that although the high *p*-CAN selectivity was preserved at 99%, the specific activities decreased dramatically to 0.24×10^4, 0.56×10^4 and 0.20×10^4 $mol_{p\text{-CNB}}\cdot mol_{Pt}^{-1}h^{-1}$ for the Au_7Pt_1, Au_3Pt_1 and Au_3Pt_2 alloy catalysts, respectively (Fig. 5a). Compared with Au@Pt core–shell catalysts, substantial reduction of the number of platinum atoms on the surface of AuPt alloys could be the main reason for the much reduced activity (Supplementary Table 4). These results again agree well with the theoretical prediction (Supplementary Table 3) and the literature[27].

Calculations of the formation rates of *p*-CAN showed that the 2.7 nm-Pt catalyst showed the highest initial rate of 0.87×10^4 $mol_{p\text{-CAN}}\cdot mol_{Pt}^{-1}h^{-1}$ among the monometallic platinum catalysts. However, this catalyst also produced a considerable amount of by-product AN (Fig. 1a) and deactivated quickly during recycling (Fig. 5d), obscuring the limited improvement in activity. Therefore, varying platinum particle size is not practical for hydrogenation of *p*-CNB. In sharp contrast, the Au@1ML-Pt catalyst achieved a *p*-CAN formation rate of 3.41×10^4 $mol_{p\text{-CAN}}\cdot mol_{Pt}^{-1}h^{-1}$, along with 99% selectivity and good recyclability, far superior to all the catalysts reported (Supplementary Table 7).

In addition to the above findings, we further showed that Au@1ML-Pt also exhibited remarkable activity improvements along with 99% HAN selectivity in hydrogenation of *m*-CNB and *p*-BNB compared with all platinum monometallic catalysts (Supplementary Table 8). More importantly, this strategy of a monolayer core–shell bimetallic catalyst might be general although the optimized shell thickness might slightly vary for different systems. A similar remarkable improvement in both activity and chemoselectivity was also found on Au@Pd core–shell catalysts in hydrogenation of *p*-CNB, where Au@0.5ML-Pd showed optimal performance (Supplementary Figs. 35 and 36 and Supplementary Table 9).

Conclusions

We have demonstrated in this article that the activity and selectivity of chemoselective hydrogenation of HNBs to HANs over Pt/SiO_2 catalysts showed a see-saw relationship with platinum particle size. Theoretical calculations revealed that the geometric effect plays the major role for larger platinum NPs, where the hydrogenation path occurs on platinum terrace sites, and the undesired dehalogenation path preferentially occurs on low-coordination sites. On smaller platinum clusters, however, the electronic effect becomes remarkable, reversing the above trend of activity and selectivity. In sharp contrast, for bimetallic monolayer Au@1ML-Pt core–shell catalysts, a considerable ligand effect and lattice stretch of the platinum shell induced by the gold core substantially shift the platinum shell *d*-band centre toward the Fermi level, while preserving the terrace sites for high selectivity. These changes improve the reaction energetics and facilitate the reaction kinetics, respectively, breaking the above trade-off limitation by achieving a remarkable activity along with a high HAN selectivity of >99%. Finally, the properties of the distinct geometric and electronic structures of bimetallic monolayer core–shell catalysts revealed here not only point out a promising way to design highly chemoselective and active metal catalysts, but also highlight the importance of quantifying their independent contribution over activity and selectivity as a general principle for rational catalyst design.

Methods

Chemicals and materials. Trimethyl(methylcyclopentadienyl)platinum(IV) ($MeCpPtMe_3$, >99%) was purchased from Strem Chemicals. The silica support (Brunauer–Emmett–Teller surface area, 300 m^2g^{-1}) and palladium(II) hexafluoroacetylacetonate ($Pd(hfac)_2$, >97%) were purchased from Sigma-Aldrich. $HAuCl_4{\cdot}4H_2O$ (>99%), tetraamminepalladium(II) chloride monohydrate ($Pd(NH_3)_4Cl_2{\cdot}H_2O$, 99%), ammonia solution ($NH_3{\cdot}H_2O$, 25–28%) and ethanol (>99.5%) were purchased from Sinopharm Chemical Reagent. *p*-CNB (>99%), *m*-CNB (>99%), *p*-BNB (>99%) and *m*-xylene (>99%) were purchased from Aladdin. All gases including ultrahigh-purity N_2 (99.999%), Ar (99.999%) and O_2 (99.999%), and the mixtures of 10% O_2, 10% H_2 and 10% CO in Ar (or He) were all provided by Nanjing Special Gases. All of the chemicals were used as purchased without further purification.

Synthesis of Pt/SiO_2 catalysts. Platinum ALD was carried out on silica support to synthesize the platinum catalysts in a viscous flow ALD reactor (ALD-V401-PRO, ACME (Beijing) Technology) using ultra-high-purity (UHP) N_2 as a carrier gas at a flow rate of 200 ml min^{-1} (ref. [29]). The $MeCpPtMe_3$ precursor was heated to 65 °C to achieve a sufficient vapour pressure and UHP O_2 was used as the oxidant. Platinum ALD was performed for two ALD cycles at 250 °C to obtain the 2.7 nm-Pt catalyst, where the timing sequence was 200, 300, 100 and 300 s for the $MeCpPtMe_3$ exposure, N_2 purge, O_2 exposure and N_2 purge, respectively. To vary the particle size, the ALD temperature was changed. The 2.1 nm-Pt and 1.1 nm-Pt catalysts were prepared at 200 and 150 °C, respectively, using the same timing sequence, while the 4.3 nm-Pt, 6.1 nm-Pt and 9.3 nm-Pt catalysts were obtained by calcining the 2.7 nm-Pt catalyst in 10% O_2 in Ar at 550 °C for 1 h, 600 °C for 1 h and 600 °C for 2 h, respectively. All catalysts were calcined in 10% O_2 in Ar at 150 °C for 30 min and then reduced at 150 °C for another 30 min in 10% H_2 in Ar before any characterization and reaction tests.

Synthesis of 5.3 nm-Au and $Au@Pt/SiO_2$ bimetallic catalysts. To achieve selective platinum deposition on gold NPs instead of SiO_2 support for the later synthesis of $Au@Pt/SiO_2$ core–shell bimetallic catalysts, here spherical SiO_2 support was synthesized according to the modified Stöber method[47] and further calcined in 10% O_2 in Ar at 700 °C for 3 h to remove most of the surface hydroxyl group for promotion of the selective platinum deposition.

The 5.3 nm-Au catalyst was prepared using the deposition–precipitation method as we reported previously[48]. Three millilitres of $HAuCl_4$ aqueous solution (0.0485 moles per litre), 1.0 g spherical SiO_2 and 150 ml deionized water were added together into a three-necked bottle and mixed for 30 min under vigorous stirring at 60 °C; ammonia was used to adjust the pH value to between 9 and 10. The system was stirred for another 12 h. After that the solid was centrifuged and washed with deionized water five times, and dried at 60 °C overnight. Finally, the sample was calcined at 300 °C under 10% O_2 in Ar for 2 h to obtain the 5.3 nm-Au catalyst.

To precisely synthesize $Au@Pt/SiO_2$ core–shell bimetallic catalysts, platinum ALD was performed at 150 °C to selectively deposit platinum onto the gold NPs in the 5.3 nm-Au catalyst for 1, 3 and 8 cycles, during which the platinum deposition on spherical SiO_2 was inhibited. The resulting samples were denoted as Au@0.5ML-Pt, Au@1ML-Pt and Au@2ML-Pt, respectively. In this case, the timing sequence was 30, 200, 6 and 200 s for $MeCpPtMe_3$ exposure, N_2 purge, O_2 exposure and N_2 purge, respectively.

Synthesis of $AuPt/SiO_2$ alloy catalysts. The silica-supported Au_7Pt_1, Au_3Pt_1 and Au_3Pt_2 alloy catalysts with different Au/Pt mole ratios were synthesized by annealing the Au@0.5ML-Pt, Au@1ML-Pt and Au@2ML-Pt core–shell bimetallic catalysts at 500 °C in 10% H_2 in Ar for 30 min, respectively. The formation of AuPt alloys was confirmed by X-ray diffraction and CO chemisorption.

Synthesis of Pd/SiO_2 and Au@Pd bimetallic catalysts. The Pd/SiO_2 catalysts were synthesized by the deposition–precipitation method. First, 0.007 g $Pd(NH_3)Cl_2{\cdot}H_2O$, 0.4 g silica (calcined at 700 °C under 10% O_2 in Ar for 3 h) and 125 ml deionized water were added together into a round bottom flask and mixed for 30 min under vigorous stirring at 25 °C; then ammonia was used to adjust the pH value to 12. After stirring the mixture for another 1 h, the solid was centrifuged and washed with deionized water five times, and dried at 60 °C overnight. Finally, the powder materials were reduced at 300 °C under 10% H_2 in Ar for 1 h to obtain the Pd/SiO_2 catalyst with a particle size of ~0.9 nm-Pd, which was denoted as 0.9 nm-Pd. To vary the palladium particle size, we adjusted the amount of $Pd(NH_3)Cl_2{\cdot}H_2O$ and the reduction temperature; 0.015, 0.050 and 0.080 g $Pd(NH_3)Cl_2{\cdot}H_2O$ with a reduction pretreatment of 350 °C for 1 h, 400 °C for 1 h and 400 °C for 2 h, yielded the 1.6 nm-Pd, 3.4 nm-Pd and 5.2 nm-Pd catalysts, respectively.

Similar to the synthesis of $Au@Pt/SiO_2$ core–shell bimetallic catalysts, Au@Pd core–shell bimetallic catalysts were fabricated by selectively depositing palladium onto gold NPs in the 5.3 nm-Au catalyst using palladium ALD at 150 °C for 1 and 3

cycles.[48] The resulting catalysts were denoted as Au@0.5ML-Pd and Au@1ML-Pd, respectively. Here the timing sequence was 30, 200, 15 and 200 s for $Pd(hfac)_2$ exposure, N_2 purge, H_2 exposure and N_2 purge, respectively. The $Pd(hfac)_2$ precursor was heated to 65 °C to achieve a sufficient vapour pressure. All catalysts were calcined in 10% O_2 in Ar at 150 °C for 30 min and then reduced at 150 °C for another 30 min in 10% H_2 in Ar before any characterization and reaction tests.

Morphology and composition. TEM measurements were performed on a JEM-2100F instrument operated at 200 kV to characterize the morphology of these catalysts. Elemental mapping using EDS was performed on the same equipment. STEM characterization of Au@1ML-Pt and Au@2ML-Pt bimetallic catalysts with an atomic resolution was carried out on an aberration-corrected HAADF-STEM instrument at 200 kV (JEM-ARM200F, University of Science and Technology of China). The metal contents in various catalysts were analysed by inductively coupled plasma atomic emission spectroscopy.

DRIFTS CO chemisorption measurements. DRIFTS CO chemisorption measurements were performed on a Nicolet iS10 spectrometer equipped with a mercury–cadmium–telluride detector and a low-temperature reaction cell (Praying Mantis Harrick). After loading a sample into the cell, it was first calcined in 10% O_2 in Ar at 150 °C for 30 min followed by a reduction in 10% H_2 in Ar at 150 °C for another 30 min. After cooling the sample to room temperature under a continuous flow of Ar, a background spectrum was collected. Subsequently, the sample was exposed to 10% CO in Ar at a flow rate of 20 ml min^{-1} for about 30 min until saturation. Next, the sample was purged with Ar at a flow rate of 20 ml min^{-1} for another 30 min to remove the gas-phase CO, and then the DRIFT spectrum was collected with 256 scans at a resolution of 4 cm^{-1}.

In situ XPS. In situ XPS measurements were conducted with a Thermo Scientific ESCALAB 250Xi X-ray photoelectron spectrometer equipped with high-pressure gas cell (HPGC 300, Fermi Instruments). The monochromatic Al K_α (1486.6 eV) X-ray source was used at 225 W (15 kV, 15 mA). The binding energy scale of all spectra was calibrated to the Si 2*p* peak (103.5 eV). The in situ reduction of the samples was performed in a high-pressure gas cell in 10% H_2 in Ar (20 ml min^{-1}) at 150 °C for 30 min. Next, the sample was cooled in 10% H_2 in Ar, evacuated and transferred within the spectrometer to the analyser chamber for XPS analysis without exposing it to air.

Platinum dispersion measurements. The platinum dispersions of platinum, AuPt alloy and Au@Pt core–shell catalysts were determined by CO pulse chemisorption, which was conducted on a Micromeritics AutoChem II chemisorption instrument. After loading a sample, the catalyst was first calcined in 10% O_2 in He at 150 °C for 30 min followed by a reduction in 10% H_2 in He at 150 °C for another 30 min. Then, the catalysts were cooled to room temperature in He, and CO pulses were introduced to the catalyst surface using 10% CO in He until saturation. The amount of chemisorbed CO was calibrated with a thermal conductivity detector.

Catalyst evaluation. The selective hydrogenation of *p*-CNB was carried out in a 100 ml stainless steel batch reactor. The amount of catalyst used for the reaction test was normalized to have the same platinum/substrate mole ratio of 1:7,800. Typically, *p*-CNB (8 mmol), the catalyst, *m*-xylene (8/3 mmol) and C_2H_5OH (40 ml) were loaded into the autoclave. Here *m*-xylene was used as the internal standard. Next, the autoclave was flushed with ultrahigh-purity Ar to remove the air and then heated to 65 °C under Ar. When the temperature was stabilized at 65 °C, the autoclave was pressurized with 0.3 MPa H_2. After that, the mixture was stirred at a rate of 1,500 r.p.m. to start the reaction. During the reaction, the liquid sample mixture was taken out through a sampling valve and analysed by gas chromatography (Shimadzu GC-2014, equipped with an Rtx-1 capillary column and autoinjector). The turnover frequencies (TOFs) were calculated using the following equation:

$$\mathrm{TOFs} = \frac{\text{moles of rectant converted}}{\text{moles of surface metal atoms} \times \text{reaction time}} \quad (3)$$

The specific rates were also calculated using the following equation with the total amount of platinum or palladium metals:

$$\text{specific rates} = \frac{\text{moles of rectant converted}}{\text{moles of total metal (Pt or Pd) atoms} \times \text{reaction time}} \quad (4)$$

Computational methods. Density functional theory calculations were performed using the Vienna Ab initio Simulation Package. The exchange-correlation effect was described by the Perdew–Burke–Ernzerhof functional within the generalized-gradient approximation scheme including van der Waals correction[49–51]. The Kohn–Sham equations were expanded with a plane-wave basis set with a kinetic energy cutoff of 400 eV. The metal lattice parameters were determined by PBE revised for solids (PBEsol)[52]. The core–valence interactions were treated by the projected augmented wave pseudopotentials[53]. The convergence criterion was set to 0.02 eV $Å^{-1}$ during structure optimization. The transition states of elementary reactions were located by the climbing-image nudged elastic band method and the convergence criterion was 0.05 eV $Å^{-1}$ (ref. [54]). The obtained structures were further confirmed by a single imaginary frequency along the reaction coordination. A four-layer slab in a (4×4) supercell was used to model the flat Pt(111) surface. The Pt(211) surface was modelled by a p(2×4) supercell with eight atomic layers and the bottom four atomic layers were frozen. The free-standing Pt_{55}, Pt_{147} and Pt_{309} particles were constructed using a cuboctahedron structure based on the literature and all the atoms were allowed to relax[31,55]. A 1ML-Pt/Au(111) surface was used to simulate Au@Pt core–shell NPs by supporting a platinum monolayer on a four-layer Au(111) substrate. AuPt alloy was modelled by a AuPt(111) surface with an Au:Pt ratio of 1:1 (Supplementary Fig. 18). In Pt(111), 1ML-Pt/Au(111) and AuPt(111) slabs, the bottom two layers were fixed in their bulk position while the remaining metal and all the adsorbates were allowed to relax. A vacuum of at least 20 Å was introduced along the *z* axis to avoid artificial interactions between repeated slabs/particles. A (3×3×1) Monkhorst–Pack *K*-point mesh and *Γ* point were used to sample the Brillouin zone for slabs and particles, respectively[56]. The adsorption energies of molecules were calculated as follows:

$$E_{\mathrm{ads}}(\mathrm{molec}) = E_{\mathrm{molec/slab}} - E_{\mathrm{slab}} - E_{\mathrm{molec}}(\mathrm{g}) \quad (5)$$

where $E_{\mathrm{molec/slab}}$, E_{slab} and $E_{\mathrm{molec}}(\mathrm{g})$ are the total energies of the molecule–surface system, the clean surface and the free molecule in the gas phase, respectively. The reaction energies E_r and energy barriers E_a of elementary steps were defined as $E_r = E_{FS} - E_{IS}$ and $E_a = E_{TS} - E_{IS}$, where E_{IS}, E_{TS} and E_{FS} are the total energies of the initial state, the transition state and the final state, respectively.

Data availability

The data generated during this study are included in this article (and its Supplementary Information files) or can be obtained from the authors upon reasonable request.

Received: 23 September 2020; Accepted: 30 August 2021;
Published online: 18 October 2021

References

1. Calle-Vallejo, F. et al. Finding optimal surface sites on heterogeneous catalysts by counting nearest neighbors. *Science* **350**, 185–189 (2015).
2. Calle-Vallejo, F., Loffreda, D., Koper, M. T. M. & Sautet, P. Introducing structural sensitivity into adsorption-energy scaling relations by means of coordination numbers. *Nat. Chem.* **7**, 403–410 (2015).
3. den Breejen, J. P. et al. On the origin of the cobalt particle size effects in Fischer–Tropsch catalysis. *J. Am. Chem. Soc.* **131**, 7197–7203 (2009).
4. Kuhn, J. N., Huang, W. Y., Tsung, C. K., Zhang, Y. W. & Somorjai, G. A. Structure sensitivity of carbon–nitrogen ring opening: impact of platinum particle size from below 1 to 5 nm upon pyrrole hydrogenation product selectivity over monodisperse platinum nanoparticles loaded onto mesoporous silica. *J. Am. Chem. Soc.* **130**, 14026–14027 (2008).
5. Reske, R., Mistry, H., Behafarid, F., Cuenya, B. R. & Strasser, P. Particle size effects in the catalytic electroreduction of CO_2 on Cu nanoparticles. *J. Am. Chem. Soc.* **136**, 6978–6986 (2014).
6. Englisch, M., Jentys, A. & Lercher, J. A. Structure sensitivity of the hydrogenation of crotonaldehyde over Pt/SiO_2 and Pt/TiO_2. *J. Catal.* **166**, 25–35 (1997).
7. Cao, S. W., Tao, F., Tang, Y., Li, Y. T. & Yu, J. G. Size- and shape-dependent catalytic performances of oxidation and reduction reactions on nanocatalysts. *Chem. Soc. Rev.* **45**, 4747–4765 (2016).
8. Halperin, W. P. Quantum size effects in metal particles. *Rev. Mod. Phys.* **58**, 533–606 (1986).
9. Li, L. et al. Investigation of catalytic finite-size-effects of platinum metal clusters. *J. Phys. Chem. Lett.* **4**, 222–226 (2013).
10. Wang, A. Q., Liu, X. Y., Mou, C. Y. & Zhang, T. Understanding the synergistic effects of gold bimetallic catalysts. *J. Catal.* **308**, 258–271 (2013).
11. Shi, J. L. On the synergetic catalytic effect in heterogeneous nanocomposite catalysts. *Chem. Rev.* **113**, 2139–2181 (2013).
12. Liu, L. C. & Corma, A. Metal catalysts for heterogeneous catalysis: from single atoms to nanoclusters and nanoparticles. *Chem. Rev.* **118**, 4981–5079 (2018).
13. Zhang, L. L., Zhou, M. X., Wang, A. Q. & Zhang, T. Selective hydrogenation over supported metal catalysts: from nanoparticles to single atoms. *Chem. Rev.* **120**, 683–733 (2020).
14. Zhao, M. T. et al. Metal–organic frameworks as selectivity regulators for hydrogenation reactions. *Nature* **539**, 76–80 (2016).
15. Blaser, H. U., Steiner, H. & Studer, M. Selective catalytic hydrogenation of functionalized nitroarenes: an update. *ChemCatChem* **1**, 210–221 (2009).
16. Jones, C. R., Liu, Y. Y., Sepai, O., Yan, H. F. & Sabbioni, G. Internal exposure, health effects, and cancer risk of humans exposed to chloronitrobenzene. *Environ. Sci. Technol.* **40**, 387–394 (2006).

17. Zhang, P. P. et al. Kinetically stabilized Pd@Pt core–shell octahedral nanoparticles with thin Pt layers for enhanced catalytic hydrogenation performance. *ACS Catal.* **5**, 1335–1343 (2015).
18. Liu, M. et al. Design of highly efficient Pt–SnO_2 hydrogenation nanocatalysts using Pt@Sn core–shell nanoparticles. *ACS Catal.* **7**, 1583–1591 (2017).
19. Cardenas-Lizana, F. et al. Selective gas phase hydrogenation of *p*-chloronitrobenzene over Pd catalysts: role of the support. *ACS Catal.* **3**, 1386–1396 (2013).
20. Xu, Q., Liu, X. M., Chen, J. R., Li, R. X. & Li, X. J. Modification mechanism of Sn^{4+} for hydrogenation of *p*-chloronitrobenzene over PVP-Pd/γ-Al_2O_3. *J. Mol. Catal. A Chem.* **260**, 299–305 (2006).
21. Cai, S. F. et al. Highly active and selective catalysis of bimetallic Rh_3Ni_1 nanoparticles in the hydrogenation of nitroarenes. *ACS Catal.* **3**, 608–612 (2013).
22. Wang, C. P. et al. Insight into single-atom-induced unconventional size dependence over CeO_2-supported Pt catalysts. *Chem* **6**, 752–765 (2020).
23. Corma, A. & Serna, P. Chemoselective hydrogenation of nitro compounds with supported gold catalysts. *Science* **313**, 332–334 (2006).
24. Boronat, M. et al. A molecular mechanism for the chemoselective hydrogenation of substituted nitroaromatics with nanoparticles of gold on TiO_2 catalysts: a cooperative effect between gold and the support. *J. Am. Chem. Soc.* **129**, 16230–16237 (2007).
25. Gong, H. H. et al. Atomically precise Ag nanoclusters intercalated in zirconium pyrophosphate for efficient hydrogenation of nitroaromatics. *Appl. Catal. A: Gen.* **574**, 1–9 (2019).
26. Chen, Y. Y., Wang, C. A., Liu, H. Y., Qiu, J. S. & Bao, X. H. Ag/SiO_2: a novel catalyst with high activity and selectivity for hydrogenation of chloronitrobenzenes. *Chem. Commun.* 5298–5300 (2005).
27. Serna, P., Concepcion, P. & Corma, A. Design of highly active and chemoselective bimetallic gold–platinum hydrogenation catalysts through kinetic and isotopic studies. *J. Catal.* **265**, 19–25 (2009).
28. Makosch, M. et al. Organic thiol modified Pt/TiO_2 catalysts to control chemoselective hydrogenation of substituted nitroarenes. *ACS Catal.* **2**, 2079–2081 (2012).
29. Cao, L. N. et al. Atomically dispersed iron hydroxide anchored on Pt for preferential oxidation of CO in H_2. *Nature* **565**, 631–635 (2019).
30. Wang, H. W. et al. Disentangling the size-dependent geometric and electronic effects of palladium nanocatalysts beyond selectivity. *Sci. Adv.* **5**, 8 (2019).
31. Kleis, J. et al. Finite size effects in chemical bonding: from small clusters to solids. *Catal. Lett.* **141**, 1067–1071 (2011).
32. Lu, J. L. et al. Toward atomically-precise synthesis of supported bimetallic nanoparticles using atomic layer deposition. *Nat. Commun.* **5**, 3264 (2014).
33. Baker, L. et al. Nucleation and growth of Pt atomic layer deposition on Al_2O_3 substrates using (methylcyclopentadienyl)-trimethyl platinum and O_2 plasma. *J. Appl. Phys.* **109**, 084333 (2011).
34. Le Bars, J., Specht, U., Bradley, J. S. & Blackmond, D. G. A catalytic probe of the surface of colloidal palladium particles using Heck coupling reactions. *Langmuir* **15**, 7621–7625 (1999).
35. Qiu, L. M., Liu, F., Zhao, L. Z., Yang, W. S. & Yao, J. N. Evidence of a unique electron donor–acceptor property for platinum nanoparticles as studied by XPS. *Langmuir* **22**, 4480–4482 (2006).
36. Bai, L. C. et al. Explaining the size dependence in platinum-nanoparticle-catalyzed hydrogenation reactions. *Angew. Chem. Int. Ed.* **55**, 15656–15661 (2016).
37. Wang, G. W. et al. Pt skin on AuCu intermetallic substrate: a strategy to maximize Pt utilization for fuel cells. *J. Am. Chem. Soc.* **136**, 9643–9649 (2014).
38. Singh, J., Lamberti, C. & van Bokhoven, J. A. Advanced X-ray absorption and emission spectroscopy: in situ catalytic studies. *Chem. Soc. Rev.* **39**, 4754–4766 (2010).
39. de Groot, F. High resolution X-ray emission and X-ray absorption spectroscopy. *Chem. Rev.* **101**, 1779–1808 (2001).
40. Gallezot, P., Weber, R., Dallabetta, R. A. & Boudart, M. Investigation by X-ray absorption spectroscopy of platinum clusters supported on zeolites. *Z. Naturforsch. A Phys. Sci.* **34**, 40–42 (1979).
41. Lytle, F. W. Determination of *d*-band occupancy in pure metals and supported catalysts by measurement of L_3 X-ray absorption threshold. *J. Catal.* **43**, 376–379 (1976).
42. Ding, K. et al. Identification of active sites in CO oxidation and water-gas shift over supported Pt catalysts. *Science* **350**, 189–192 (2015).
43. Wang, C. L. et al. Water-mediated Mars–Van Krevelen mechanism for CO oxidation on ceria-supported single-atom Pt_1 catalyst. *ACS Catal.* **7**, 887–891 (2016).
44. Davidson, E. R., Kunze, K. L., Machado, F. B. C. & Chakravorty, S. J. The transition-metal carbonyl bond. *Acc. Chem. Res.* **26**, 628–635 (1993).
45. Mott, D. et al. Nanocrystal and surface alloy properties of bimetallic gold–platinum nanoparticles. *Nanoscale Res. Lett.* **2**, 12–16 (2007).
46. Rodriguez, J. A. & Kuhn, M. Chemical and electronic properties of Pt in bimetallic surfaces: photoemission and CO-chemisorption studies for Zn/Pt(111). *J. Chem. Phys.* **102**, 4279–4289 (1995).
47. Bourgeat-Lami, E. & Lang, J. Encapsulation of inorganic particles by dispersion polymerization in polar media: 2. Effect of silica size and concentration on the morphology of silica–polystyrene composite particles. *J. Colloid Interface Sci.* **210**, 281–289 (1999).
48. Wang, H. W., Wang, C. L., Yan, H., Yi, H. & Lu, J. L. Precisely-controlled synthesis of Au@Pd core–shell bimetallic catalyst via atomic layer deposition for selective oxidation of benzyl alcohol. *J. Catal.* **324**, 59–68 (2015).
49. Perdew, J. P., Burke, K. & Ernzerhof, M. Generalized gradient approximation made simple. *Phys. Rev. Lett.* **77**, 3865–3868 (1996).
50. Klimes, J., Bowler, D. R. & Michaelides, A. Van der Waals density functionals applied to solids. *Phys. Rev. B* **83**, 195131 (2011).
51. Klimeš, J., Bowler, D. R. & Michaelides, A. Chemical accuracy for the van der Waals density functional. *J. Phys. Condens. Matter* **22**, 022201 (2010).
52. Perdew, J. P. et al. Restoring the density-gradient expansion for exchange in solids and surfaces. *Phys. Rev. Lett.* **102**, 1 (2009).
53. Blochl, P. E. Projector augmented-wave method. *Phys. Rev. B* **50**, 17953–17979 (1994).
54. Henkelman, G., Uberuaga, B. P. & Jonsson, H. A climbing image nudged elastic band method for finding saddle points and minimum energy paths. *J. Chem. Phys.* **113**, 9901–9904 (2000).
55. Li, L. et al. Investigation of catalytic finite-size-effects of platinum metal clusters. *J. Phys. Chem. Lett.* **4**, 222–226 (2012).
56. Methfessel, M. & Paxton, A. T. High-precision sampling for Brillouin-zone integration in metals. *Phys. Rev. B* **40**, 3616–3621 (1989).

Acknowledgements

J.L. acknowledges support from the National Natural Science Foundation of China (22025205, 21673215), the Dalian National Laboratory for Clean Energy (DNL) Cooperation Fund (DNL201907), the Fundamental Research Funds for the Central Universities (WK2060030029), and Users with Excellence Program of Hefei Science Center CAS (2019HSC-UE016). W.-X.L. acknowledges the National Key R&D Program of China (2018YFA0208603), the National Natural Science Foundation of China (91945302), the Dalian National Laboratory for Clean Energy (DNL) Cooperation Fund (DNL201920), the Chinese Academy of Sciences (QYZDJ-SSW-SLH054) and K.C. Wong Education (GJTD-2020-15). Y.L. acknowledges support from the Youth Innovation Promotion Association of the CAS (2020458). Y.Y. acknowledges support from the National Natural Science Foundation of China (22072092, 92045301). S.W. acknowledges the National Key R&D Program of China (2017YFA0402800). The authors all gratefully thank the BL14W1 beamline at the Shanghai Synchrotron Radiation Facility (SSRF) and Supercomputing Center of University of Science and Technology of China and National Supercomputing Center in Zhengzhou.

Author contributions

J.L. designed the experiments and W.-X.L. designed the DFT calculations. Q.G. synthesized and characterized the catalysts and evaluated the catalytic performance. C.Z. did the DFT calculations. Y.L. did the HAADF-STEM measurements. E.I.V., X.Z. and Y.Y. did the XPS measurements. H.Y., L.C., H.W., X.Z., X.L. and M.Z. assisted the catalyst characterization and catalytic performance evolution. S.W. performed the XAFS measurements. J.L. and W.-X.L. co-wrote the manuscript, and all the authors contributed to the overall scientific interpretation and edited the manuscript.

Competing interests

The authors declare no competing interests.

Additional information

Supplementary information The online version contains supplementary material available at https://doi.org/10.1038/s41929-021-00679-x.

Correspondence and requests for materials should be addressed to Wei-Xue Li or Junling Lu.

Peer review Information *Nature Catalysis* thanks Meenakshisundaram Sankar and the other, anonymous, reviewer(s) for their contribution to the peer review of this work.